

Hydrodynamic loading and viscous damping of patterned perforations on microfabricated resonant structures

Kidong Park, Jiwook Shim, Vita Solovyeva, Elise Corbin, Shouvik Banerjee et al.

Citation: *Appl. Phys. Lett.* **100**, 154107 (2012); doi: 10.1063/1.4704144

View online: <http://dx.doi.org/10.1063/1.4704144>

View Table of Contents: <http://apl.aip.org/resource/1/APPLAB/v100/i15>

Published by the [American Institute of Physics](#).

Related Articles

Nanoscale temperature sensing using the Seebeck effect

J. Appl. Phys. **111**, 084306 (2012)

Vimentin networks at tunable ion-concentration in microfluidic drops

Biomicrofluidics **6**, 022009 (2012)

Note: Adhesive stamp electrodes using spider silk masks for electronic transport measurements of supra-micron sized samples

Rev. Sci. Instrum. **83**, 046106 (2012)

Covalently immobilized biomolecule gradient on hydrogel surface using a gradient generating microfluidic device for a quantitative mesenchymal stem cell study

Biomicrofluidics **6**, 024111 (2012)

High-performance microfluidic rectifier based on sudden expansion channel with embedded block structure

Biomicrofluidics **6**, 024108 (2012)

Additional information on *Appl. Phys. Lett.*



Journal Homepage: <http://apl.aip.org/>

Journal Information: http://apl.aip.org/about/about_the_journal

Top downloads: http://apl.aip.org/features/most_downloaded

Information for Authors: <http://apl.aip.org/authors>

ADVERTISEMENT

INSTRUMENTS FOR ADVANCED SCIENCE				
	Gas Analysis dynamic measurement of reaction gas streams catalysis and thermal analysis molecular beam studies dissolved species probes fermentation, environmental and ecological studies	Surface Science UHV TPD SIMS end point detection in ion beam etch elemental imaging - surface mapping	Plasma Diagnostics plasma source characterisation etch and deposition process reaction kinetic studies analysis of neutral and radical species	Vacuum Analysis partial pressure measurement and control of process gases reactive sputter process control vacuum diagnostics vacuum coating process monitoring
	contact Hiden Analytical for further details: info@hiden.co.uk www.HidenAnalytical.com CLICK TO VIEW OUR PRODUCT CATALOGUE			
				

Hydrodynamic loading and viscous damping of patterned perforations on microfabricated resonant structures

Kidong Park,^{1,2} Jiwook Shim,^{1,2} Vita Solovyeva,^{1,2} Elise Corbin,^{2,3} Shouvik Banerjee,^{2,4} and Rashid Bashir^{1,2,5,a)}

¹Department of Electrical and Computer Engineering, University of Illinois at Urbana-Champaign, Urbana, Illinois 61801, USA

²Micro and Nanotechnology Laboratory, University of Illinois at Urbana-Champaign, Urbana, Illinois 61801, USA

³Department of Mechanical Science and Engineering, University of Illinois at Urbana-Champaign, Urbana, Illinois 61801, USA

⁴Department of Material Science and Engineering, University of Illinois at Urbana-Champaign, Urbana, Illinois 61801, USA

⁵Department of Bioengineering, University of Illinois at Urbana-Champaign, Urbana, Illinois 61801, USA

(Received 24 February 2012; accepted 24 March 2012; published online 13 April 2012)

We examined the hydrodynamic loading of vertically resonating microfabricated plates immersed in liquids with different viscosities. The planar structures were patterned with focused ion beam, perforating various shapes with identical area but varying perimeters. The hydrodynamic loading of various geometries was characterized from resonant frequency and quality factor. In water, the damping increased linearly with the perimeter at 45.4×10^{-3} Ns/m², until the perforation's radius was $123\% \pm 13\%$ of the depth of penetration of fluid's oscillation. The added mass effect decreased with perforations and recovered to the level of un-perforated structures when the perforation's radius became smaller than the depth of penetration. © 2012 American Institute of Physics. [<http://dx.doi.org/10.1063/1.4704144>]

Mechanically resonating structures have been widely used in microelectromechanical systems (MEMS) as sensors.¹⁻⁴ Quality factor, defined as the ratio of the energy loss per cycle to the total stored energy of a resonating structure, is an important parameter characterizing the resonance. With a higher quality factor, resonant sensors can exhibit higher sensitivity and resonators can vibrate with larger amplitude while consuming less energy. When the resonant structure is immersed in viscous fluid, the quality factor and the resonant frequency decrease dramatically due to the viscous damping and the added mass effect from the surrounding fluid.⁵ For this reason, many MEMS sensors^{6,7} and ultrasensitive nanomechanical resonant mass sensors^{8,9} are operated in a low pressure environment for maximum performance. However, providing such low-pressure environment increases the manufacturing cost and could limit the practical use of the sensors in fluid. Moreover, uncompromised operations in biological buffers are frequently required for atomic force microscopy and many other bio-MEMS devices.

There have been a number of theoretical and experimental investigations on the effect of the fluid viscosity and the device geometry on quality factor of resonating MEMS structures. In earlier studies, a theoretical frequency response model of the cantilever beam immersed in viscous fluid was developed^{5,10} and various studies¹¹⁻¹⁴ have elucidated the hydrodynamic loading on the cantilevers in viscous liquid. Vančura *et al.* investigated the added mass and the viscous damping of magnetically driven cantilevers of different

dimensions in pure water, glycerol, and ethanol solutions.¹¹ The effect of the surrounding fluid on the resonance of atomic force microscopy cantilevers was characterized, and the discrepancy of the measured damping to the theoretical estimation was reported.¹³ Also, a finite element-based numerical model revealed that the dissipation mechanism in viscous fluid originated from localized fluid shear near the edge of the vibrating structure.¹⁴ Vibrating MEMS plates with evenly distributed perforations are routinely found in commercial MEMS devices, and the resonant characteristic of such structures has been investigated in order to characterize the squeeze film effect¹⁵ and the viscous damping in air or low-pressure environment.¹⁶⁻¹⁹ However, previous studies were focused on modeling the hydrodynamic loading of specific geometries, such as cantilevers or perforated plates, and the effect of the geometric parameters on the hydrodynamic loading has not been experimentally investigated in detail. In this paper, the effect of the geometry of the perforation on the hydrodynamic loading was characterized. Various sizes and number of holes were formed in microfabricated rectangular plates suspended by four folded springs. The quality factor and the resonant frequency were measured to extract the viscous damping and the “added mass” due to various geometries.

The MEMS mass sensors developed in an earlier study²⁰ were perforated with focused ion beam (FIB) to make through-holes with various dimensions. The folded springs that connect to the rectangular plate converted part of the flexural bending of the springs into the torsional bending and evenly distributed the deflection, minimizing the spatial variation of the modal displacement on the plate.²¹ The variation of the modal displacement on the plate was less than 2.0%

^{a)} Author to whom correspondence should be addressed. Electronic mail: rbashir@illinois.edu.

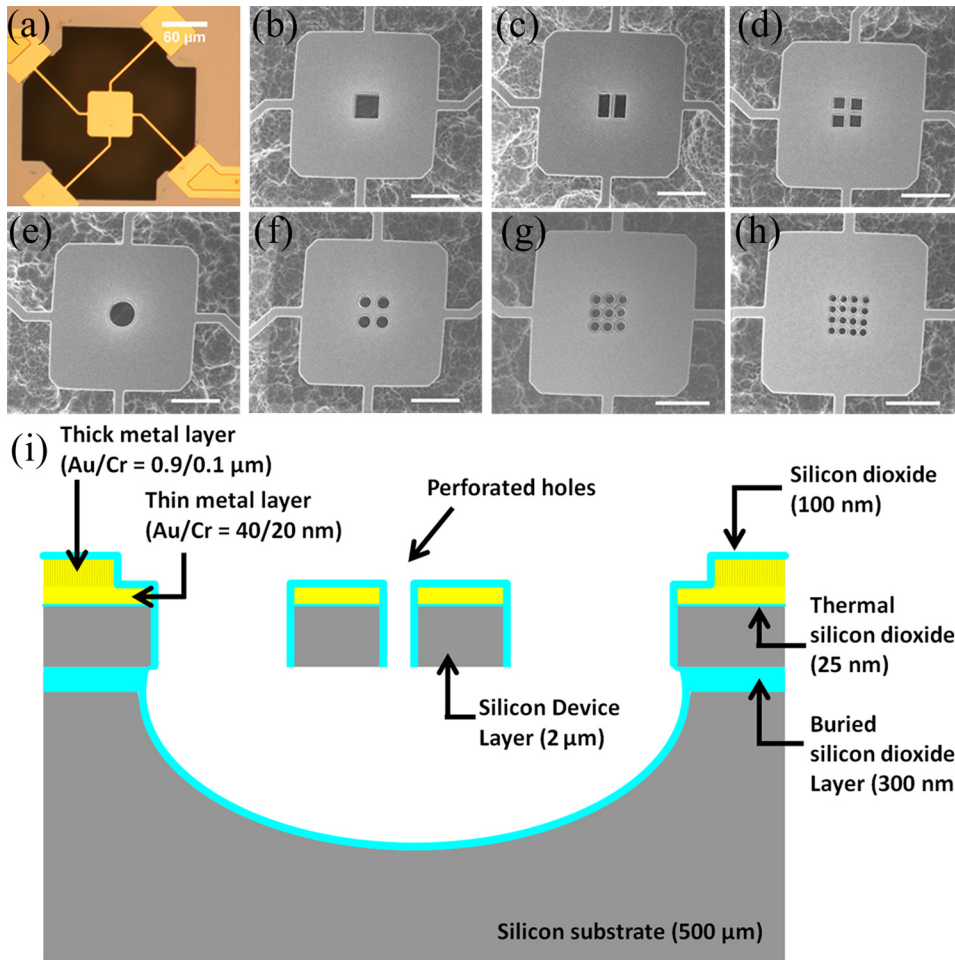


FIG. 1. (a) Optical image of the MEMS device, before perforation with FIB. Scale bar: $60\ \mu\text{m}$. (b)–(h) The scanning electron microscope (SEM) image of the perforations for groups 1–7 in Table II, respectively. Scale bar: $20\ \mu\text{m}$. (i) Cross-sectional diagram of the perforated device.

based on finite element analysis, and the modal displacement was experimentally measured to be spatially uniform on the plate.²² The device before the FIB process is shown in Fig. 1(a), and the devices after the FIB process are shown in Figs. 1(b)–1(h). The cross-sectional diagram of the device after perforation is shown in Fig. 1(i). The rectangular plate is $2\ \mu\text{m}$ in thickness and $60\ \mu\text{m} \times 60\ \mu\text{m}$ in area, and there is a cavity of more than $50\ \mu\text{m}$ in depth beneath the plate. Therefore, the frequency response of the device was not affected by the “squeeze-film” effect. A polydimethylsiloxane (PDMS) microfluidic well with a top glass cover was attached on top of the device. A magnetic field over $0.1\ \text{T}$ was applied to the device, and the device was actuated with Lorentz force by applying an alternating current through the device. The plate velocity was optically measured with a laser Doppler vibrometer (LDV) and further analyzed with a lock-in-amplifier. Detailed information on the fabrication and the experimental setup is described in the previous report.²⁰

The device immersed in liquid can be modeled as a second-order harmonic oscillator, as shown in

$$m\ddot{X}(j\omega) + c\dot{X}(j\omega) + kX(j\omega) = F_{ext}(j\omega), \quad (1)$$

where $X(j\omega)$, m , c , k , ω , and F_{ext} were displacement, mass, damping coefficient, spring constant, angular velocity, and Lorentz force, respectively. In this work, the resonant frequency, f_r , is defined as $f_r = \frac{1}{2\pi} \sqrt{\frac{k}{m}}$. The mass, m , includes the effective mass of the structure and the added mass

from the surrounding liquid. The resonant frequency is obtained by finding the frequency at which the velocity output of the LDV was in phase to the applied actuation current, as in

$$j\omega X(j\omega) \left[c + j\omega \left(m - \frac{k}{\omega^2} \right) \right] = F_{ext}(j\omega), \quad (2)$$

where $j\omega X(j\omega)$ is the velocity.

The quality factor, Q , was extracted from the measured slope of the velocity phase, Φ , near the resonant frequency based on²³

$$Q = \frac{f_r}{2} \frac{d\Phi}{df}, \quad (3)$$

where the slope of the velocity phase was extracted from the measured phase difference of the velocity at two frequencies, i.e., $500\ \text{Hz}$ higher and $500\ \text{Hz}$ lower than the resonant frequency of the device.

One of the key parameters to characterize the oscillation of the viscous fluid near a resonating solid object is the depth of penetration.²⁴ The velocity of the viscous fluid in close vicinity of the resonating surface is the same as that of the surface and decreases exponentially away from the surface. The depth of penetration, δ , is the distance over which the velocity decays by a factor of $1/e$ ($e \approx 2.7183$) of the peak value, and dependent on the kinematic viscosity, ν , and the resonant frequency, f_r , as shown in

TABLE I. Mechanical properties of the liquids used in the study.

	Density ρ (g cm ⁻³)	Dynamic viscosity η (g m ⁻¹ s ⁻¹)	Kinematic viscosity ν (cm ² /s)
DI water	0.9982	1.002×10^{-2}	1.0038×10^{-2}
9% glucose solution	1.0334	1.289×10^{-2}	1.2473×10^{-2}
18% glucose solution	1.0710	1.757×10^{-2}	1.6405×10^{-2}

$$\delta = \sqrt{\frac{2\nu}{2\pi f_r}}. \quad (4)$$

The hydrodynamic loading of the perforated devices were measured with three different liquids, deionized (DI) water, 9%, and 18% glucose dissolved in DI water (w/v) to provide different viscosity values. The viscosity and the density of the liquids²⁵ are presented in Table I. According to Eq. (4) and Table I, the depth of penetration in DI water, and the 9% and 18% glucose solution are 2.29, 2.57, and 3.00 μm , respectively.

The geometries of the perforations were carefully designed so that the change of the hydrodynamic loading could be clearly observed. The perforation radius was chosen between 1.41 μm and 6.04 μm , ensuring the depth of penetration to lie within the range of the perforation radius. Also, these geometries were chosen to have the identical perforated area of 100 μm^2 but varying perimeter ranging from 35.4 μm to 141.7 μm . The radius for a rectangular perforation was defined as the average of the shortest and longest distance to the perforated edge from the center of each perforation. The shortest distance was between the closest side and the center of the perforation, and the longest distance was between one of the apexes and the perforation center. For example, the radius of a rectangular perforation with 5 μm width and 10 μm height was 4.05 μm ($= (2.5 + \sqrt{2.5^2 + 5^2})/2$). The detailed dimensions are shown in Table II.

The spring constant of each device was measured before and after the FIB process to confirm that the perforation did not change the spring constant of the device. The spring constant was extracted from the mass calculated from the geometry and the resonant frequency measured in air, using

$$k = 4\pi^2 m f_{air}^2, \quad (5)$$

where f_{air} is the resonant frequency measured in air. The extracted spring constants before and after the FIB process showed little difference. The spring constants of perforated

TABLE II. Dimensions of the perforations. W and H are the width and the height of rectangular perforation. D is the diameter of circular perforation.

Group number	Perimeter (μm)	Radius (μm)	Dimension (μm)
1	40	6.04	W = H = 10
2	60	4.05	W = 5, H = 10
3	80	3.02	W = H = 5
4	35.4	5.64	D = 11.28
5	70.9	2.82	D = 5.64
6	95.3	1.88	D = 3.76
7	141.7	1.41	D = 2.82

devices were decreased by only 0.40%, whereas those of the un-perforated devices were decreased by 0.19%.

The quality factors of the various perforated and un-perforated devices are shown in Fig. 2. Since the perforations in each geometry had an identical area of 100 μm^2 , the perimeter or the total length of the perforated edges can be a good measure to describe the size of individual perforations. Larger perimeter leads to a smaller diameter of the perforations. The quality factors and the resonant frequencies were measured with DI water, 9%, and 18% glucose solution. As shown in Fig. 2, the quality factors decreased with the perforation in all three cases. With increased viscosity, the quality factors of the perforated structures were reduced by $8.8\% \pm 1.8\%$ and $15.4\% \pm 3.2\%$ for the 9% and 18% glucose solutions, respectively, whereas those of the un-perforated structures were reduced by $11.4\% \pm 0.6\%$ and $20.6\% \pm 0.3\%$ for 9% and 18% glucose solutions, respectively. The average resonant frequency of the structures was 60.8 ± 2.7 kHz in DI water, 59.8 ± 1.7 kHz in 9% glucose, and 58.0 ± 1.6 kHz in 18% glucose solution. As shown in Fig. 2, the quality factor was clearly affected by the perimeter of the perforation and the quality factors were lowest when the perimeter was around 60–80 μm . Also, it can be noted that the quality factor at 60 μm became smaller than the quality factor at 80 μm , as the viscosity increased. From these observations, it can be suggested that the quality factor is closely related to the size of individual perforations and the viscosity of the surrounding fluid.

To further analyze the effect of the perforation on the hydrodynamic loading, the damping coefficient and the mass were extracted from the quality factor and the resonant frequency, based on

$$c = \frac{\sqrt{mk}}{Q}, \quad (6)$$

$$m = \frac{1}{4\pi^2} \frac{k}{f_r^2}. \quad (7)$$

The damping coefficient and the mass in three different liquids are plotted in Fig. 3. The points at 0 μm perimeter in

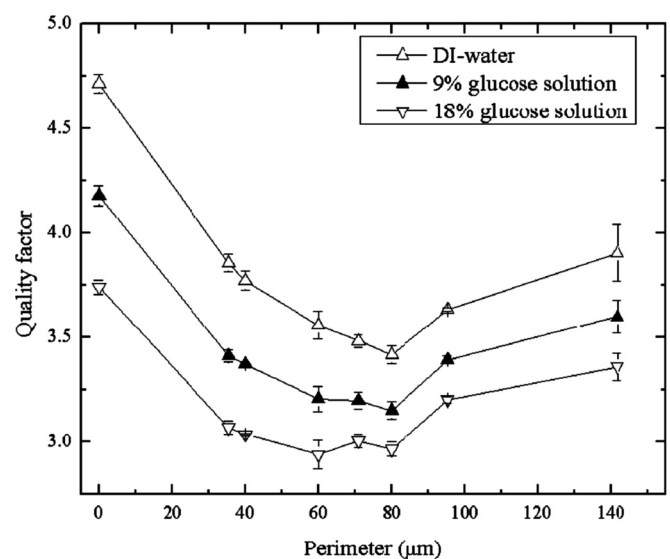


FIG. 2. Quality factors of the devices in DI water and in 9% and 18% glucose solutions. The data points at 0 μm perimeter are from the un-perforated structures.

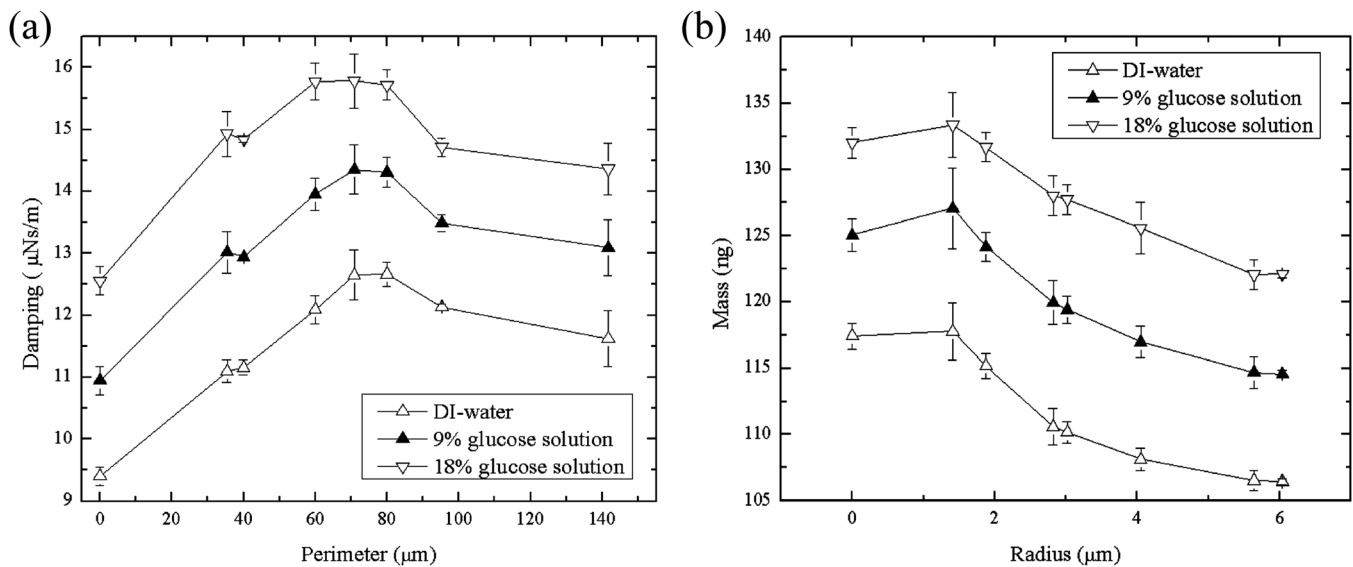


FIG. 3. Hydrodynamic loading of the devices in DI water, 9% and 18% glucose solutions. (a) Damping coefficients of the devices. (b) Mass of the devices.

Fig. 3(a) are from the measurement of the un-perforated structures. The damping coefficient of the un-perforated structure was smallest, and the damping increased linearly as the perimeter increased. Since the modal shape of the plate was essentially flat in resonance as described earlier, the additional shear and damping were considered to be originated only from the edges of the perforations. The damping coefficients in DI water and 9% glucose solution were found to saturate when the perimeter was $70.9\ \mu\text{m}$ (radius was $2.82\ \mu\text{m}$). In 18% glucose solution, the saturation was observed at $60\ \mu\text{m}$ perimeter (radius was $4.05\ \mu\text{m}$). Overall, the damping coefficients saturated with smaller perimeter or larger perforation at higher viscosity. The average ratio of the depth of penetration to the radius at which the damping coefficient became maximum was $123\% \pm 13\%$. Further increase in the perimeter after the saturation point actually decreased the damping coefficient. The damping coefficients of the perforated structures increased by $14.0\% \pm 2.2\%$ and $26.9\% \pm 4.9\%$ for the 9% and 18% glucose solutions, respectively, whereas those of the un-perforated structures increased by $16.4\% \pm 0.9\%$ and $33.6\% \pm 0.5\%$, respectively. The damping coefficients per unit length, extracted from the linear regions of the damping coefficients before the saturation, were found to be 45.4 , 48.1 , and $50.4\ \text{mNs/m}^2$ for DI water, 9%, and 18% glucose solutions, respectively.

The extracted mass with respect to the perforation radius is shown in Fig. 3(b). The added mass effect was found to be the lowest when the radius of the perforation was the largest. The added mass monotonically increased as the radius became smaller, even if the total perforated area remained constant. With the smallest perforation radius, the mass recovered to the level of the un-perforated structures. This general trend of the induced mass was maintained with increased viscosities.

The observed characteristics of the hydrodynamic loading of the various patterned-perforations can be qualitatively explained by the following consideration. If the perforation was large enough, the fluid's velocity profile generated by the vibration of the perforated edge decayed farther from the edge and practically vanishes before the perforated edge on

the other side. Therefore, the damping coefficient per unit length remained constant regardless of the perforation size and the damping coefficient increased linearly with the perimeter. When the perforation was smaller than the depth of penetration, the velocity profile generated by one perforated edge affected the velocity profile from the edge on the other side. Since both edges vibrate at same phase, the overlapping of the velocity profiles can lead to constructive interference and induces more fluid to move together with the structure, resulting in less viscous damping. For this reason, the damping coefficient decreases even with increasing perimeter. Similarly, the fluid in the middle of a large perforation becomes stationary and less amount of fluid is moving with the structure, lowering the fluid's inertial loading to the structure. At smaller perforations, more fluid is actuated by the structure and the mass increases. With a higher viscosity, the depth of penetration also increases and the velocity profile reaches farther from the perforated edge. Therefore, the saturation of the damping coefficient could be observed with larger perforation, as previously described.

In conclusion, the hydrodynamic loading on the planar structures with various patterns of perforations having identical area, but varying perimeter was experimentally characterized. It was found that the relative size of the perforations with respect to the depth of penetration was a key factor that determined the viscous damping and the added mass effect. The added mass effect was dependent on perforations size, and smaller perforations showed a higher added mass. The damping increased linearly with the perimeter with larger perforations. If the size of the perforations became similar to or smaller than the depth of penetration, the damping decreased with increasing perimeter. These observations have an implication in optimizing the resonance characteristics of complex MEMS structures operating in viscous fluid.

We acknowledge the support of National Science Foundation (NSF) Grant No. EEC-0425626 (NSF Nanoscale Science and Engineering Center at Ohio State University to R.B.), NSF Grant No. CBET-0939511 (R.B.), and funding

support from UIUC. E.A.C. was funded at UIUC from NSF Grant No. 0965918 IGERT: training the next generation of researchers in Cellular and Molecular Mechanics and BioNanotechnology. We thank Dr. Larry J. Millet at University of Illinois at Urbana-Champaign for his valuable suggestions.

- ¹P. S. Waggoner and H. G. Craighead, *Lab Chip* **7**(10), 1238 (2007).
- ²D. J. Young, İ. E. Pehlivanoglu, and C. A. Zorman, *J. Micromech. Microeng.* **19**, 115027 (2009).
- ³S. E. Alper and T. Akin, *J. Microelectromech. Syst.* **14**(4), 707 (2005).
- ⁴R. Sunier, T. Vancura, Y. Li, K.-U. Kirstein, H. Baltes, and O. Brand, *J. Microelectromech. Syst.* **15**(5), 1098 (2006).
- ⁵J. E. Sader, *J. Appl. Phys.* **84**(1), 64 (1998).
- ⁶B. Lee, S. Seok, and K. Chun, *J. Micromech. Microeng.* **13**, 663 (2003).
- ⁷M. Esashi, *J. Micromech. Microeng.* **18**, 0730001 (2008).
- ⁸K. Jensen, K. Kim, and A. Zettl, *Nat. Nanotechnol.* **3**, 533 (2008).
- ⁹Y. T. Yang, C. Callegari, X. L. Feng, K. L. Ekinici, and M. L. Roukes, *Nano Lett.* **6**(4), 583 (2006).
- ¹⁰J. W. M. Chon, P. Mulvaney, and J. E. Sader, *J. Appl. Phys.* **87**, 3978 (2000).
- ¹¹C. Vančura, I. Defour, S. M. Heinrich, F. Josse, and A. Hierlemann, *Sens. Actuators, A* **141**, 43 (2007).
- ¹²T. Adrega, V. Chu, and J. P. Conde, *Appl. Phys. Lett.* **89**, 143109 (2006).
- ¹³A. Maali, C. Hurth, R. Boisgard, C. Jai, T. Cohen-Bouhacina, and J.-P. Aime, *J. Appl. Phys.* **97**, 074907 (2005).
- ¹⁴S. Basak, A. Raman, and S. V. Garimella, *J. Appl. Phys.* **99**, 114906 (2006).
- ¹⁵M. Bao and H. Yang, *Sens. Actuators, A* **136**, 3 (2007).
- ¹⁶G. Schrag and G. Wachutka, *Sens. Actuators, A* **111**, 222 (2004).
- ¹⁷G. D. Pasquale, T. Veijola, and A. Soma, *J. Micromech. Microeng.* **20**, 015010 (2010).
- ¹⁸T. Veijola, G. D. Pasquale, and A. Soma, *Microsyst. Technol.* **15**, 1121 (2009).
- ¹⁹P. Y. Kwok, M. S. Weinberg, and K. S. Breuer, *J. Microelectromech. Syst.* **14**(4), 770 (2005).
- ²⁰K. Park, L. J. Millet, N. Kim, H. Li, X. Jin, G. Popescua, N. R. Aluru, K. J. Hsia, and R. Bashir, *Proc. Natl. Acad. Sci. U.S.A.* **10**, 20691 (2010).
- ²¹K. Park, N. Kim, D. T. Morissette, N. R. Aluru, and R. Bashir, "Resonant MEMS Mass Sensors for Measurement of Microdroplet Evaporation," *J. Microelectromech. Syst.* (in press).
- ²²K. Park and B. Rashid, in *Proceedings of the 15th International Conference on Solid-State Sensors, Actuators, and Microsystems*, Denver, Colorado, 21–25 June 2009, p. 1956.
- ²³B. Razavi, *IEEE J. Solid-State Circuits* **31**(3), 331 (1996).
- ²⁴L. D. Landau and E. M. Lifshitz, *Fluid Mechanics* (Addison-Wesley, Reading, MA, 1959).
- ²⁵W. M. Hanes, *CRC Handbook of Chemistry and Physics*, 92nd ed. (CRC, Boulder, CO, 2011).